

The Effect of Mud Cracking on the Performance of Thick Li-Ion Electrodes

Will J. Dawson,^[a, b] Andrew R. T. Morrison,^[a, b] Francesco Iacoviello,^[a] Adam M. Boyce,^[b, c] Gargi Giri,^[a, b, d] Juntao Li,^[a, b, d] Thomas S. Miller,^[a] and Paul Shearing^{*[b, d]}

Electrode-level fracture, or mud cracking, occurs during the drying process of Li-ion electrodes and is known to be particularly prevalent in thick electrodes. Whilst these cracks are generally viewed as an obstruction to the production of thicker, more energy dense electrodes, cracks are similar in structure to directional pore channels which have been proposed as a means of improving ion transport to produce thicker electrodes more capable of performing at higher rates. However, existing

literature has not thoroughly investigated the influence of cracking on the performance of electrodes. Here we analyse the 3D structure of thick cracked electrodes for the first time, using X-ray computed tomography. We show that mud cracking enhances the performance of Li-ion electrodes at discharge rates above 1 C and evaluate the implications on ion transport of different crack geometries by analysis of Euclidian distance maps.

Introduction

Lithium-ion batteries (LIBs) are ubiquitous in portable electronic applications, and are of increasing relevance to the automotive industry and short term grid storage to balance supply fluctuations from intermittent green energy sources.^[1,2] Improvements in volumetric and gravimetric energy density are likely to improve uptake of these technologies, which are crucial for the energy transition. One means of achieving improved volumetric and gravimetric energy at the cell level is by increasing electrode thickness, which reduces the proportion of inactive components such as the current collector.^[3–5] However, thick electrodes suffer from reduced proportional capacity utilisation as a result of Li-ion transport limitations. Capacity utilisation can be improved by increasing porosity within a standard architecture, or by utilising novel low-tortuosity electrode structures with directional or multiscale porosity.^[4–8] However, the former comes at the expense of volumetric energy density, and the latter typically involves additional or

alternative manufacturing methods, which would add cost to the process.

A range of such methods have been proposed to produce electrodes with directional pore structures to aid ion transport. Bae *et al.* fabricated optimised directionally-porous structures based on tortuosity modelling by co-extrusion of LiCoO₂ with a sacrificial binder phase. They achieved a more than two-fold improvement in capacity vs a homogeneous reference at 2 C, but relied on an expensive multi-stage heat treatment process including sintering at 1000 °C.^[9] Directional ice templating (DIT) similarly uses a pore-forming phase in the form of ice crystals grown through the electrode thickness, and has been demonstrated in a number of Li-ion cathode chemistries as well as graphite anodes and sulfur electrodes.^[10–19] Using DIT, electrodes as thick as 900 μm and with active material contents up to 99.5 wt.% have been demonstrated by Huang and Yang respectively.^[11,17] Magnetic alignment is a technique which produces pore channels either by the magnetic functionalisation of active materials, or by the use of magnetically active pore-forming phases such as hollow carbon fibres, to which a magnetic field is applied, resulting in the formation of directional porosity.^[20–23] Others have employed mechanical pore punching,^[24] spray coating,^[25] acoustic field-assisted particle patterning,^[26] and laser patterning.^[27–31] The latter of these is the most advanced in its development, having been studied in both anodes and cathodes, with improvements in cycle life, fast charging and electrolyte wetting.^[28,29,31] Laser patterning has also been applied to high throughput roll-to-roll processing, with a minimal increase in process cost.^[30]

Mud cracking draws its name from the process whereby cracks form during drying or shrinkage of soils, and has been observed in a range of synthetic materials such as thin films, plastics and ceramic films, which are often particulate in nature.^[32–38] Mud cracking in the context of a battery electrode refers to electrode-level fracture (as opposed to the fracture of active particles^[39–41]) where crack lengths and widths are on the order of 10s of microns wide and 100s of microns in length.

[a] W. J. Dawson, A. R. T. Morrison, F. Iacoviello, G. Giri, J. Li, T. S. Miller
Electrochemical Innovation Lab, Department of Chemical Engineering,
University College London, London WC1E 7JE, UK

[b] W. J. Dawson, A. R. T. Morrison, A. M. Boyce, G. Giri, J. Li, P. Shearing
The Faraday Institution, Quad One, Harwell Science and Innovation
Campus, Didcot OX11 0RA, UK
E-mail: p.shearing@ucl.ac.uk

[c] A. M. Boyce
School of Mechanical and Materials Engineering, University College Dublin,
Dublin D04 V1 W8, Ireland

[d] G. Giri, J. Li, P. Shearing
The ZERO Institute, University of Oxford. Holywell House, Osney Mead,
Oxford OX2 0ES

Supporting information for this article is available on the WWW under
<https://doi.org/10.1002/batt.202400260>

© 2024 The Authors. Batteries & Supercaps published by Wiley-VCH GmbH.
This is an open access article under the terms of the Creative Commons Attribution License, which permits use, distribution and reproduction in any medium, provided the original work is properly cited.

Mud cracking can occur spontaneously during the electrode drying process, and is believed to be due to capillary pressure. It therefore presents an opportunity to introduce directional porosity without significantly altering production processes.^[42] This cracking process is generally distinct from cracking which has been observed as a result of expansion and contraction during lithiation cycles in silicon and thin film Li-ion electrodes.^[43,44] This manuscript is focused on the mud cracking process, and the generic term cracking used hereon denotes cracks arising from the drying process.

Understanding cracking is of particular importance in thick slurry-coated electrodes. Singh and Tirumkudulu developed a relationship which states that for drying colloidal films under given formulation conditions there is a critical thickness above which cracking occurs.^[45] This principle was shown to hold for Li-ion battery anodes by Kumbberg *et al.* and others have shown that further increasing the electrode thickness (as well as drying temperature) increases the intensity of cracking.^[42,46–49] In addition, severe crack formation is seen as a major hindrance to the production of aqueous-processed Li-ion cathodes. Cracking severity is substantially increased by bubbles which form due to the reaction of hydroxide ions with the aluminium current collector, as well as by the high surface tension of water and the lesser ability of aqueous binder systems to withstand drying stresses.^[46,47,50]

Whilst cracking may result in mechanical weakness of the electrode, it also reduces tortuosity and thus improves ionic diffusion through the electrode. Whilst Rollag *et al.* observed some reduction in performance with increased cracking, these were aqueous electrodes with very severe cracks.^[50] Bryntesen *et al.* published the most direct analysis of the impact of cracking on electrode performance to date, and their data showed that electrodes with the highest degree of cracking had substantially better discharge capacity at C-rates between 2 C and 5 C.^[49] The authors noted, however, that the lack of analysis of the crack structure below the electrode surface limited understanding, and they did not investigate the impact of cracking over a wide range of electrode thicknesses. In this work we present a three-dimensional analysis of electrode crack structure and correlate this with electrode discharge performance at a range of C-rates. In doing so we demonstrate the potential of cracking as a low cost approach to introduce low-tortuosity channels and improve performance at higher C-rates. Cracked Li-ion cathodes of between 70–270 µm are prepared using an NMP-PVDF binder system and a tailored formulation and imaged in 3D using lab-scale X-ray computed tomography, alongside optical microscopy of surface features. Cracking characteristics in 2D and 3D are compared, and these data are related to the cathode discharge rate performance.

Methodology

Preparation of Li-ion Cathodes and Coin Cells

Positive electrode slurries were prepared with the active material $\text{LiNi}_{0.6}\text{Mn}_{0.2}\text{Co}_{0.2}$ (NMC622, BASF), conductive additive

carbon black (C-Nergy Super C65, Timcal) and polyvinylidene fluoride (PVDF) binder (Solef, Solvay Specialty Polymers) with N-methyl pyrrolidone (NMP, anhydrous 99.5%, Sigma Aldrich) as the solvent. Two formulations, one tailored to produce cracking (C) and one standard benchmark formulation (S) as in Lu *et al.* are detailed in Table 1.^[51] Cracking was induced by increasing C65 content, while PVDF content is also increased to achieve desirable flow properties. PVDF was added gradually to stirred NMP to prevent agglomeration and the mixture was stirred overnight until fully dissolved to give an 8 wt.% solution. C65 was added to this solution, alongside half of the volume of additional NMP required to give the desired solid content, and mixed in a planetary mixer (Thinky ARE-250, Intertronics) for 1 minute at 500 rpm and 5 minutes at 2000 rpm. NMC622 was then added alongside the remaining NMP and mixed for 10 minutes at 2000 rpm with 3 minutes degassing at 2200 rpm in the planetary mixer. Coatings of various thicknesses ranging from 60–270 µm were prepared (Table S1) using a calibrated doctor blade (Elcometer 3600/4) and draw down coater (Elcometer 4340) and dried on a hotplate at 60 °C for at least 4 hours. Cathode discs of 14.9 mm diameter and separator discs of 19 mm diameter (Celgard 2325) were cut using a punch. Electrodes, separators and CR2032 type coin cell parts including top, bottom, gasket, spring and 1 mm spacer disc were dried under vacuum for a minimum of 24 h. The separator and gasket were dried at 60 °C whilst all other components were dried at 100 °C, before coin cell assembly under an argon atmosphere, using 100 µL of 1 M LiPF_6 in a solvent consisting of a 30:70 wt.% ethylene carbonate:ethyl methyl carbonate mixture with 2 wt.% vinylene carbonate as electrolyte, and a manual 2032 coin cell crimper (Hohsen).

Coin Cell Cycling

Electrochemical rate capability testing was carried out using a BCS-805 Battery Cycler (Biologic). After cells were manufactured as described above and rested for a minimum of 3 hours, two formation cycles were carried out with constant current charge at C/20 of theoretical maximum capacity followed by constant voltage until the current fell below C/40. After a five minute rest, cells were discharged at constant current of C/20, which was followed by a 60 minute rest. Capacity was re-calculated from formation cycles and used for the rate capability testing regime. For testing, cells were charged and discharged symmetrically at 5 rates in ascending order: C/10, C/2, 1 C, 2 C and 4 C. Cells were charged at constant current of the assigned C-rate to a cut off of 4.3 V, followed by a constant voltage period until current fell below C/20. Then following a 5 minute rest, cells were discharged at the set C-rate until the voltage fell below 2.8 V. After each discharge there was a 1 h rest, and each charge/discharge rate was repeated a total of 5 times before progressing to the next rate.

X-ray Computed Tomography

Discs of Li-ion cathodes of 3 mm diameter were cut using a micro-milling laser (A Series/Compact Laser Micromachining System, Oxford Lasers) and imaged in triplicate using an X-ray micro-CT system (Xradia 620 Versa, Zeiss). The 3 mm discs were imaged with the x-ray source set to 110 kV and 10 W with 4x magnification, giving voxel sizes of between 1.6 μm and 1.71 μm . Exposure time was 2 s for each of 1601 projections. X-ray projection files were reconstructed with a cone beam reconstruction algorithm in Scout and Scan Control System Reconstructor (Zeiss). Centre shift values were tailored to individual images and beam hardening constant of 1 was used for all samples. Reconstructed images were cropped using Avizo (Avizo3D 2022.1, ThermoFisher) to give an analysed field of view of ca. 1.85 \times 1.85 mm and to remove the current collector below, and void region above the electrode.

All volumes were segmented using the open-source software iLastik in pixel classification mode with all features selected.^[52,53] The segmentation process is shown in Figure S4, where initial phase labelling was carried out on 7 2D slices within the volume, after which clear errors in the segmentation were corrected by additional labelling until a satisfactory result was achieved for each volume. Cracks were identified as being objects of 50 μm^3 or greater. This size limit was determined on the basis that very fine and shallow objects with the appearance of cracks were present at the upper electrode surface, and fine cracks are often fragmented into multiple smaller objects after segmentation. Percolation in the z-direction was calculated in triplicate using the axis connectivity module in Avizo, applied to the cropped, segmented electrode images. Euclidian distance maps from the crack regions were calculated in Avizo, first removing all crack regions which were not directly connected to the upper electrode surface, since these do not directly facilitate rapid ion transport through the thickness. These maps represent the distance of any given point from the nearest crack in an individual 2D slice of the volume.

Optical Microscopy

Cathode coin cell discs prepared as described above were imaged prior to coin cell construction with a digital optical microscope (VHX-7000, Keyence). A magnification of 50x was used alongside 'depth up' z-stacking to bring the whole image into focus and image stitching to image the full electrode area (15 mm dia.). This allowed for the analysis of a much larger area than by SEM without sacrificing the ability to discern and segment cracks. Images were saved as 2D TIFs and segmented using iLastik as described above for X-ray CT images. Pixel size at the given magnification was determined by measuring the lengths of lines drawn within the Keyence analytical software, and dividing by the number of pixels. These measurements were carried out at in triplicate for each electrode, and the pixel size was 2.0 μm^2 in all cases. Objects of 40 μm^2 or greater were labelled as cracks, on the basis of that the smallest visually identified crack objects were of this size.

Results and Discussion

Two- and Three-dimensional Analysis of Crack Geometry

As has been shown previously, the formation of mud cracks during the electrode drying process is influenced by the thickness of the electrode coating. Cracking intensity factor (CIF) is a metric which describes ratio of surface crack area to total surface area, expressed here as a percentage.^[34] 3D CIF is a new metric used here, which similarly describes the ratio of crack volume to the overall volume of the sample, determined here by analysis of X-ray computed tomographic reconstructions, which are shown in Figure 2. For clarity, the cracking intensity factors determined from single 2D slices from these 3D volumes (Figure 2) are hereon referred to as 2D CIFs.

Figure 1 shows optical micrographs of electrodes prepared according to the formulation C (Table 1) of mean dry thicknesses increasing from 71 μm to 269 μm . The thinnest of these coatings (electrode C1, Figure 1a) had very minimal cracking, with a CIF of 0.37%, which increased to 3.37% for the thickest coating (electrode C4, Figure 1d). For electrodes of intermediate thicknesses of 129 μm and 196 μm (electrodes C2 and C3, Figure 1b and c) changes in CIF are minimal (from 1.20% to 1.39%) and within the standard deviation, indicating that there may not be a significant difference between the 2D CIF values for intermediate thickness electrodes. For the thickest electrodes (269 μm) CIF increased substantially from 1.39% to 3.37%, and so the s-shape of the relationship between dry electrode thickness and CIF indicates that there may be two critical thicknesses, above which cracking becomes more severe.

The 3D CIF values show a similar pattern to CIF, but the 3D CIF values are higher for all thicknesses: 1.08% for C1, 1.92% for C2, 1.71 for C3 and 4.19% for C4, which are higher than the 2D CIFs of the same electrodes by 0.71%, 0.72%, 0.31% and 0.83% respectively. In the intermediate thicknesses of C2 and C3 there is a reduction of 3D CIF from 1.91% to 1.71% (Figure 1b and c), with this change again within the standard deviations of the two points. Differences between CIF and 3D CIF are to be expected since the majority of crack volume is sub-surface, and surface features are unlikely to be identical to global 3D characteristics. However, given that cracks narrow through the thickness towards the current collector, it might be expected that the CIF of the surface exceeded the 3D CIF. This difference may result from differences in imaging and processing methods, but may also reflect an inability of surface characterisation to fully capture cracking on an uneven surface. This

Table 1. Details of the electrode slurry formulations used in the study, where formulation C is tailored to produce cracking, and formulation S serves as a standard reference.

Formulation	Mass of Solid Components/%			Total Solid Content/%
	NMC 622	C65	PVDF	
C	87	5	8	40
S ⁵¹	96	2	2	60

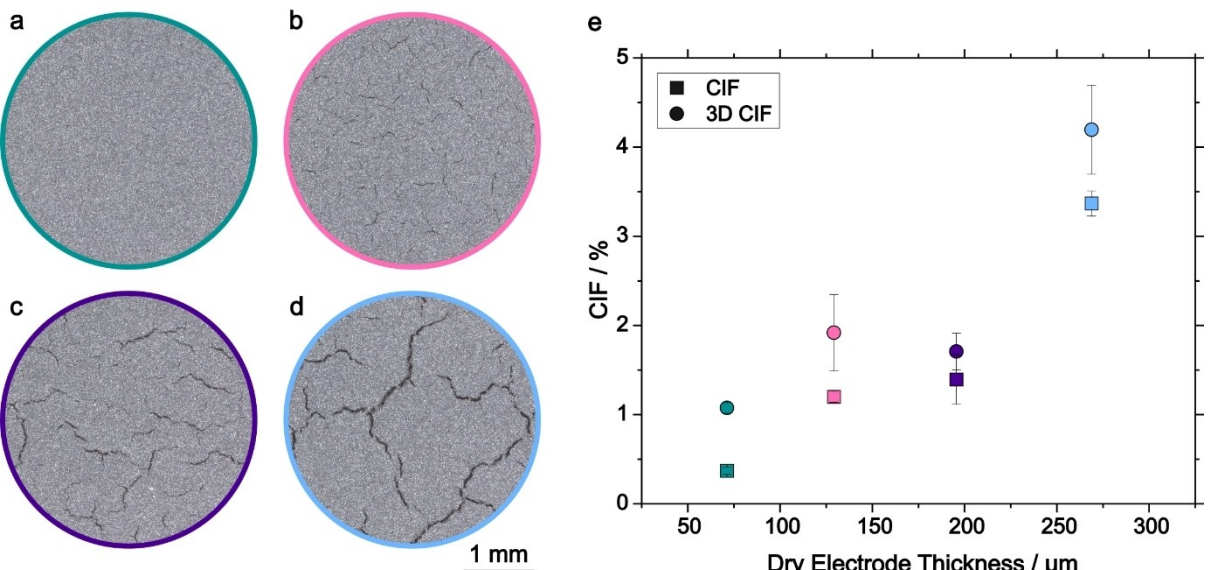


Figure 1. Representative optical micrographs showing electrodes (a) C1, (b) C2, (c) C3, (d) C4; alongside corresponding 2D and 3D cracking intensity factors, where the 3D CIF is derived from X-ray computed tomography imaging. Error bars indicate the standard deviation of the measured datasets.

highlights the value of 3D characterisation, and this discussion is expanded on below in relation to Figure 2. Larger standard deviations for 3D CIF than for CIF are observed for electrodes C2 and C4. These may be explained by the smaller sample sizes for XCT imaging (3 mm rather than 14.9 mm for optical microscopy) and fewer sampling repeats resulting in less representative datasets (Table S2).

Figure 2 shows representative XCT reconstructed volumes of electrodes C1–4 (Figure 2a, c, e and g respectively) alongside isolated renderings of the crack region (Figure 2b, d, f, h) which correspond to Figure 1 a-d and are detailed in Table S1. The slice-by-slice evolution of the 2D CIFs for these volumes as a function of distance from the current collector are shown alongside (Figure 2i, j). 2D CIF evolution data for all volumes are given in Figure S3. Looking first at the 3D renderings, we see clearly that as electrode thickness increases, individual cracks appear wider and deeper, in agreement with optical microscopy data. Renderings of the crack structure (Figure 2b, d, f, h) show that alongside cracks, the segmentation process includes some larger pore regions within the crack phase. These larger pores are to be expected, since the electrodes are not calendered. For the thinnest electrode, C1 (Figure 2a, b), these pores appear to constitute the majority of 'crack' volume, but the prevalence of these large pores reduces as electrode thickness increases, and electrode C4 (Figure 2g, h) has far fewer such structures. The 'crack' region is dominated in the thickest electrodes by genuine cracks. This suggests that the expansion of cracks during the drying process results in a compression of the adjacent electrode, reducing general porosity and concentrating porosity within the cracks. This may limit ion transport outside of the cracks to the extent that electrode performance is reduced.

In Figure 2i, it can be seen that for all thicknesses, the 2D CIF reduces initially between 0–20 μm from the current

collector, before increasing. This effect is particularly pronounced for electrode C2 (Figure 2c, d). This pattern may result from a degree of delamination at the base of the cracks in some cases, and it is believed there is also a baseline cracking measurement which results from larger pore regions still present due to the absence of calendering. After the initial reduction, 2D CIF increases with distance from the current collector for all samples, although gradually for thicker electrodes. Electrode C2 (Figure 2c, d) exhibits a 2D CIF higher at all points than electrode C3 (Figure 2e, f), which alongside the greater CIF close to the current collector explains the higher 3D CIF of C2 than C3 seen in Figure 1. The more rapid decrease in the 2D CIF for electrodes C1 and C2 suggests that cracks reach less far from the surface. By contrast electrodes C3 and C4 have many cracks which visibly reach the current collector, providing an ion transport pathway through the full electrode thickness.

In Figure 2i it is also noted that the final electrode thickness is less than the measured electrode thicknesses given in Table S1. This is because it was necessary to crop out regions at the top and bottom of the electrodes to fully remove the current collector and limit the impact of surface roughness on the data (process described in detail in the methods section). For electrode C1 (Figure 2a, b), which is the thinnest, this resulted in a loss of around half of the total thickness – the applicability of this methodology is therefore more limited for thin electrodes. Loss of material in cropping can be limited by ensuring a smooth coating with a properly calibrated doctor blade; and keeping the sample flat by adhesion to a flat sample mount oriented in parallel with the centre of the x-ray beam. It is also notable that the 2D CIFs measured at the surface of each electrode are substantially higher than the corresponding CIFs from optical microscopy (Figure 1). An example of this trend is shown in Figure 2j, in which the 2D CIF evolution through electrode thickness of electrode C4 (Figure 2g, h) is plotted with

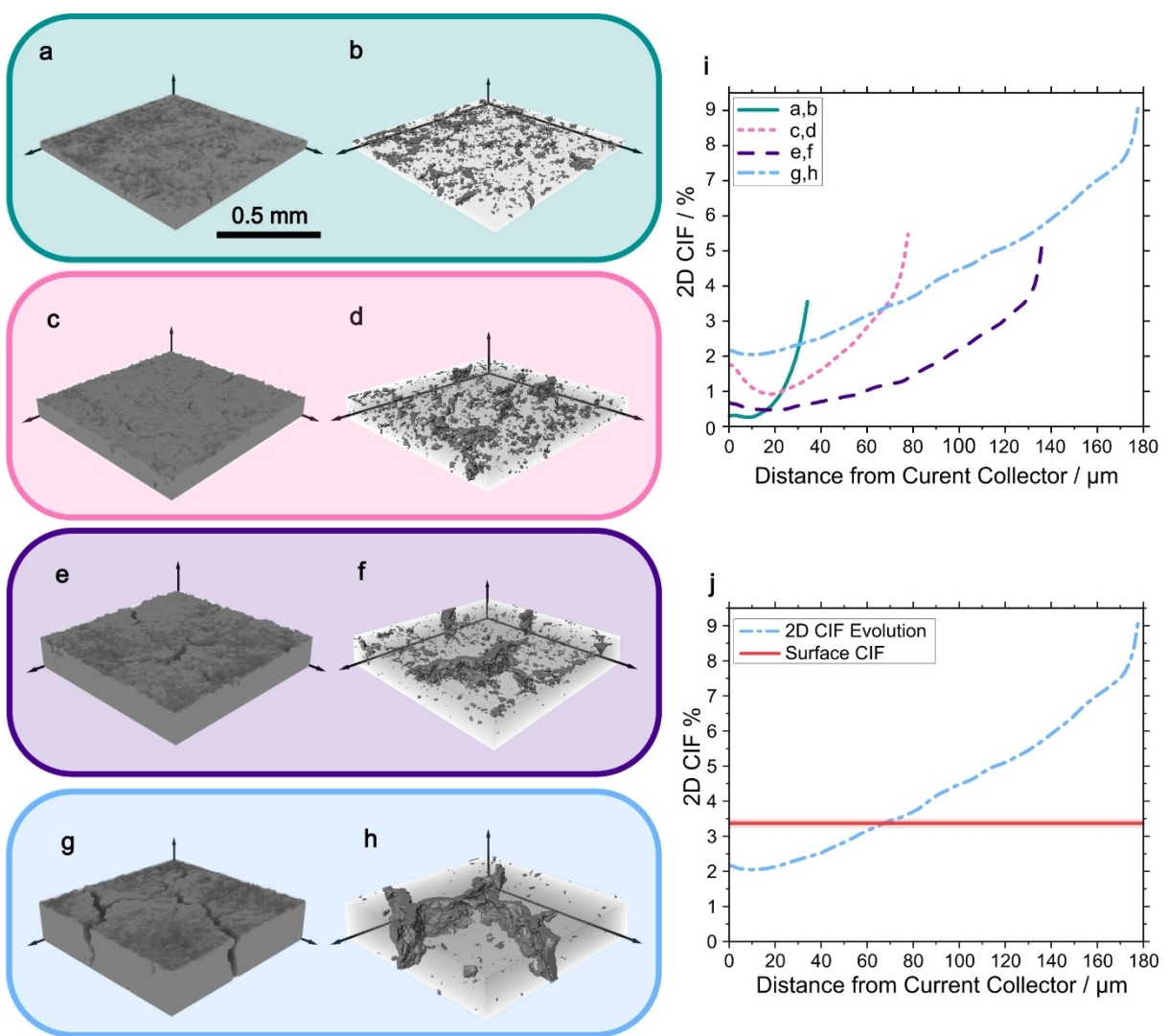


Figure 2. Subvolumes of reconstructed X-ray tomographs, of 925 μm square and varying thicknesses, showing 3D structure and isolated crack regions for electrodes (a,b) C1, (c,d) C2, (e,f) C3 and (g,h) C4; alongside graphs showing (i) the slice-by-slice evolution of CIF for each electrode as a function of distance from the current collector; and (j) 2D CIF evolution of electrode C4 determined from X-ray CT data alongside the surface CIF calculated from optical micrographs, with standard deviation indicated by the shaded area.

the corresponding surface CIF determined by optical microscopy (Figure 1d). While the 2D CIF measured from X-ray CT data increases to 9.05 % at the upper electrode surface, the CIF from optical microscopy is $3.37 \pm 0.14\%$. Some of this discrepancy results from differences in image processing methodologies. 3D volumes must be cropped slightly below the top surface in order to limit the amount of free space above the electrode which is included in 2D CIF and 3D calculations. Inevitably, however, some of this volume will be present and increase overall 3D CIF. Nonetheless, as seen in Figure 3, single-slice CIFs exceed the surface 2D CIF well before the surface of the electrode, and this observation is consistent across all electrode thicknesses. It is likely that, due to the uneven surface of the electrode, some of the surface cracking is obscured from the path of optical light. X-ray imaging overcomes this limitation, providing a more thorough picture of the intensity of

cracking at the surface as well as through the full electrode thickness.

It is evident that not all changes in the morphology of cracks which result from changes in electrode thickness are captured by 2D and 3D CIF metrics. Further analysis of cracking is shown in Figure 3 which shows the mean size (Figure 3a) and frequency of cracks (Figure 3b), as well as the percentage of crack volume which percolates through the full z-direction. Based on visual observation of cracking characteristics, it was expected that the mean crack size (area and volume) would increase and number of cracks would decrease as the electrode thickness was increased. For both the 2D and 3D cases the former prediction is reflected in the data, with the mean crack area and volume mirroring the pattern observed for 2D and 3D CIFs. A plateau between electrodes C2 and C3 is seen, with increases in crack size on either side. The very large increase in crack area and volume between electrodes C3 and C4 indicate

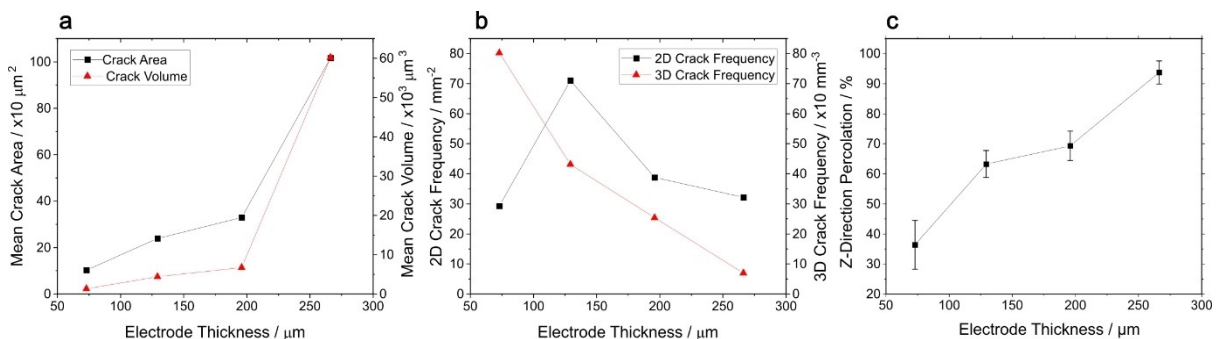


Figure 3. Graphs showing (a) mean crack area and volume as a function of electrode thickness; (b) areal and volumetric crack frequency, determined by optical microscopy and X-ray CT respectively; and (c) percentage of crack volume which percolates through the full electrode thickness (z-direction). Error bars in (c) indicate the standard deviation of the three measured volumes, while for (a) and (b) datasets were combined, so no standard deviation is presented.

that there may be a critical thickness above which catastrophic cracking occurs.

The general trend of increased crack size is consistent with previous reports, which showed that where overall cracking intensity is increased, due to factors including electrode thickness, larger individual cracks are observed.^[49,50] This work demonstrates that this relationship holds in three dimensions. However, the trends observed in the cracking frequency (number of cracks per unit area and volume) do not follow a consistent pattern. Cracks per unit area increase from 29 to 71 mm⁻² between electrodes C1 and C2, whereas cracks per unit volume decrease from 8000 to 4200 mm⁻³. As has been observed in other materials, when coating thickness increases the electrode material exceeds a critical cracking thickness and cracks form spontaneously.^[45] A large number of cracks form at the surface, but as seen in Figure 2, the cracks in electrode C1 and C2 tend to be shallow, so this increase in cracking is only observed in the surface CIF data. Changes in 3D cracking frequency are also obscured by the high initial 3D cracking frequency, due to the presence of a large number of small voids which are erroneously identified as cracks, seen in Figure 2. As genuine cracking increases with increased coating thickness in electrodes C3 and C4, these voids are reduced as larger cracks take up more of the volume, and so the 3D cracking frequency reduces. This reduction continues as cracks begin to agglomerate into fewer, larger cracks in C3 and C4. The size and number of cracks are relevant to the impact on Li-ion transport and therefore electrode performance. Cracks which penetrate the full electrode thickness, as is most likely for the thickest electrode, C4, provide a rapid ion transport pathway through to the current collector. However, the fewer, larger cracks in electrode C4 provide a more spatially heterogeneous arrangement of pore channels with greater horizontal distances between channels. This heterogeneity may limit the positive impact of enhanced ion transport. The fine-tuning of these inter-related characteristics may allow for optimised performance.

The trend in percolation (Figure 3c), determined by analysis of x-ray CT images, also followed the same s-shaped trend as cracking intensity. The thinnest electrode (C1) has a mean z-direction percolation of 36%, while for electrode C4 mean z-

direction percolation is 94%. The plateau at intermediate electrode thicknesses is between 63% and 69% for electrode C2 and C3 respectively. That crack percolation increases in line with crack intensity implies that cracks are most likely to open at or near the electrode surface, and grow downwards through the electrode thickness. The percolation in the x- and y-directions (parallel to the current collector) was analysed and in all cases found to be 0%, so it can be concluded that cracks primarily increase ion transport in the through-thickness direction, with limited increases parallel to the current collector along the path of the crack.

To evaluate the impact of cracking on the ion transport through the full electrode, analysis of Euclidian distance maps is presented below. The maps, which are shown in Figure S5, represent the distance from each voxel to nearest crack voxel. It therefore enables an analysis of the extent to which cracks are likely to influence a given region of the electrode by reducing diffusion distance. Plots of characteristic diffusion times (t_{diff}) vs diffusion distance are shown in Figure S6, which were calculated using Equation S1 to inform analysis of the Euclidian distance maps. We estimate the porosity of cracked, uncalendered electrodes to be 50.3%, a mean value of the 6 uncalendered electrode porosities in Usseglio-Viretta *et al.*^[54] The diffusion coefficient was taken to be $3 \times 10^{-6} \text{ cm}^2 \text{ s}^{-1}$, which is in line literature measurements taken at room temperature.^[55,56] Literature tortuosity factors (τ) determined from image analysis range widely between 1.5–6, with uncertainties including type of imaging, whether the carbon-binder domain is accounted for, image segmentation method and the subjectivity of the individual carrying out the analysis.^[53,54,57,58] Here we plot curves corresponding to τ values of 3 and 6 at a porosity of 50.3%, this being the most common range of values. We also plot a curve where the porosity and tortuosity are taken as 20% and 6 respectively (since low porosity typically results in high tortuosity) to correspond to the analysis of state of lithiation gradients through electrode thickness by Li *et al.*^[59] However, diffusion is complex, influenced by a number of factors including electrochemical kinetics, Ohmic factors, ions present in the electrolyte and concentration gradients (per Fick's first law). As a result of this complexity, literature analyses of the state of lithiation by

experiment and image-based modelling show results which differ from those implied by characteristic diffusion time alone.^[7,59] With this qualification, in Figure 4 we analyse the Euclidian distance maps shown in Figure S5.

If cracks which are connected to the surface have a tortuosity of near 1, and a porosity of 100%, the characteristic diffusion time of Li⁺ travelling a distance of 250 μm would be 3.5 minutes, and only 8 seconds for a distance of 50 μm. Given this enhanced diffusion through cracks, they act in practice in a similar fashion to the bulk electrolyte at the electrode surface, and their presence therefore has a profound impact on ion transport pathways. Cracks can be considered near-equivalents of the electrode surface, and in-plane diffusion through the electrode microporosity is the transport rate determining step. In Figure 4a, the distance to the nearest crack, d_{crack} , is compared with the distance to the surface, d_{surf} , plotting the proportion of the electrode where crack distance is greater than surface distance at four depths within the electrode, plotted as a percentage distance from the current collector to normalise for the varying thicknesses of electrodes. This plot represents the relative influence of through-plane (d_{surf}) and in-plane (d_{crack}) diffusion on Li-ion availability in the electrode. For electrode C1, since it is relatively thin, more than 90% of the electrode is closer to the electrode surface than the nearest crack at all depths, which corresponds to 5–10% of the electrode where in-plane diffusion is likely to have a greater influence. Electrodes C2 and C3 show similar trends, with a minimum of 80% of the electrode slice area which is closer to the electrode surface than a crack, at the current collector. Both remain approximately level, between 80% and 85%, up to 62% of the distance from the current collector, with maxima of 95% and 93% for electrode C2 and C3, respectively, at 95% distance from the current collector. At the current collector of the thickest electrode, C4, an average of 49% of the electrode is closer to the surface than the nearest crack, suggesting that through-

and in-plane diffusion have a roughly equal influence on electrode lithium availability. This increases to 63% two thirds of the distance to the surface, and 91% at the electrode surface. These data suggest that, given that in almost all cases the through-plane diffusion predominates, more dense crack spacing may aid homogeneity of lithium concentration in the electrode when cycling.

Figure 4b shows the proportion of the electrode which is greater than 215 μm from the nearest crack, which equates to a 15 minute (fast charge) diffusion time at a porosity of 50% and tortuosity of 3 (Figure S6). At the upper surface of all electrodes this value is near 0%, from which level electrode C1 increases to 34% at the current collector, only very marginally higher than the thicker electrode C2. From the lower z-direction percolation of C1 than C2 (Figure 3c) it can therefore be deduced that C1 has narrower but similarly-distributed cracks at the current collector. The thickest electrode, C4, has a similar proportion of electrode regions where t_{diff} is greater than 15 minutes to C3 at 2/3 through the electrode thickness. Whilst C4 increases by 20% (from 18% to 38%), C3 increases from 16% to 59%, the majority of the electrode at the current collector having a t_{diff} greater than 15 minutes, the highest proportion of all electrodes. This implies that C3 has the greatest in-plane diffusion distances, which relates to the fact that C3 has a lower frequency of cracks compared with C2 (Figure 3b), lower mean crack volumes than C4 (Fig. 3a), as well as cracks which are lesser in volume at the current collector than C4 (Figure 2i). It should be noted, however, that electrode C3 is itself thinner than the 215 μm which this time equates to (whereas C4 is thicker). These results, accepting the limitations of t_{diff} , indicate an interplay of factors such as density of cracking, crack volume and crack depth, with the potential to be optimised for electrode performance.

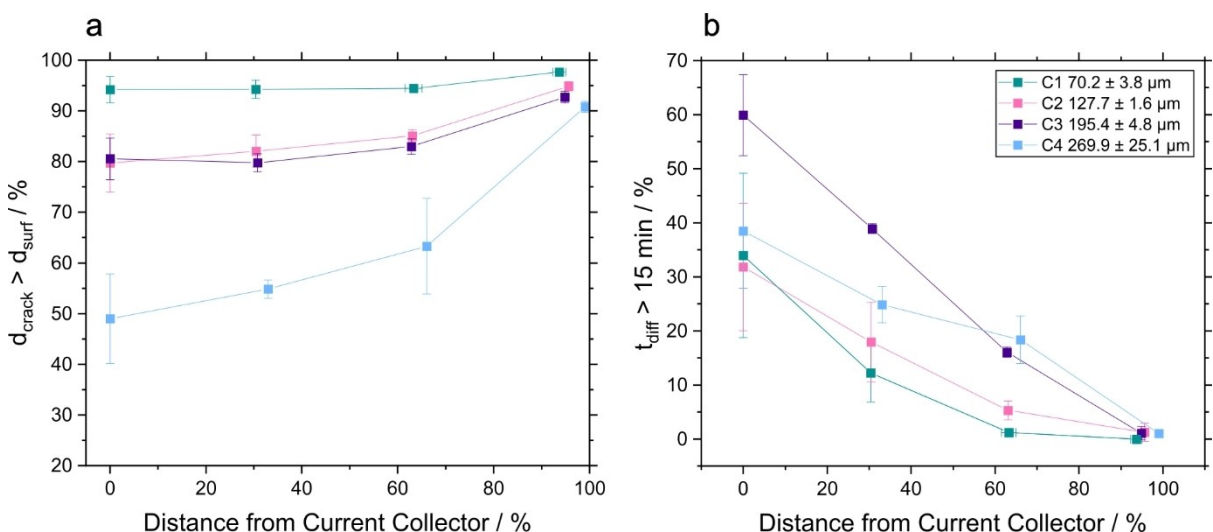


Figure 4. Plots showing analysis of 2D Euclidian distance maps of slices through the electrode thickness for electrodes C1–4, showing (a) the proportion of the electrode slice where the distance to the nearest crack voxel is greater than that to the electrode surface as a function of distance from the current collector and (b) the proportion of the electrode slice where characteristic diffusion time (t_{diff}) in-plane is greater than 15 minutes. Data points correspond to the 2D distance maps shown in Figure S5.

Electrochemical Rate Capability

Figure 5 shows cathode discharge rate performance for cracked (formulation C) and uncracked (formulation S) cathodes of a range of thicknesses (Table S1). Initial gravimetric capacities at C/10 for uncracked samples (170 mAh g^{-1} for S1) were uniformly higher than for cracked samples (151 mAh g^{-1} for C1) because the formulation had a higher NMC content (Table 1). However, as C-rate increased, the cracked samples improved their relative performance. At 2 C performance deteriorated substantially such that electrodes above $190 \mu\text{m}$ for both formulations (C3-4 and S3-4) had negligible gravimetric capacities, but those of cracked electrodes C1 and C2 were 46% and 349% higher, respectively, than capacities of corresponding uncracked electrodes S1 and S2. At 4 C electrode C1 retained 77.7% of initial gravimetric capacity, compared with 9.5% retention for electrode S1. It therefore appears that for conventional and moderately thick electrodes the presence of cracking enhances discharge capacity at C-rates of 1 C and above.

The thickest cracked electrode, C4, performed most poorly with an initial gravimetric capacity (at C/10) 4.7% lower than electrode C1 and 12.3% lower than electrode S4. At 1 C its capacity retention fell to 1.2%. This poor performance may result from a high degree of cracking impeding electrical conductivity within the electrode, and delamination preventing current flow to the current collector, as well as constriction of pore volume outside of cracks increasing tortuosity and limiting Li ion transport. For the next thickest cracked electrode, C3,

capacity retention between C/10 and C/2, capacity retention was 74.3% compared with 90% for electrode S3. However, at 1 C electrode performance was better in the cracked electrode, which retained 30.8% of initial capacity, compared with 9.3% retention in electrode S3. We propose that at lower C-rates electronic conductivity limited the performance of electrode C3, so it performed less well than the uncracked electrode. As C-rate increased to 1 C and above, ionic conductivity had a greater contribution to performance and electrode C3 began to out-perform uncracked electrode S3.^[48]

As was expected similar trends are observed for volumetric capacities, where C4 underperformed all other electrodes at C/10 and lost all capacity at 1 C. Surprisingly, electrode S1 had a far higher volumetric capacity than all other cells at C/10, 30.3% higher than S2. This increased capacity, which is not reflected in gravimetric capacity, is retained to various extents at higher C-rates and was consistent across repeats (Figure S2). Figure S1 shows that electrode S2 has a dry coating thickness below the trend exhibited by electrodes S2–4 in relation to their wet coating thickness, indicating a higher electrode density which explains the higher volumetric capacity. It is possible that this anomalous observation is explained by poor contact with the hotplate during drying of electrode S1 resulted in a lower drying temperature and a consequently lower dry electrode thickness, a trend observed by Rollag *et al.*^[50] Challenges with consistent heating of samples when using a hotplate emphasise the value of convective oven drying of electrodes. Despite this anomaly, at 4 C sample C1 had a volumetric capacity 386.9%

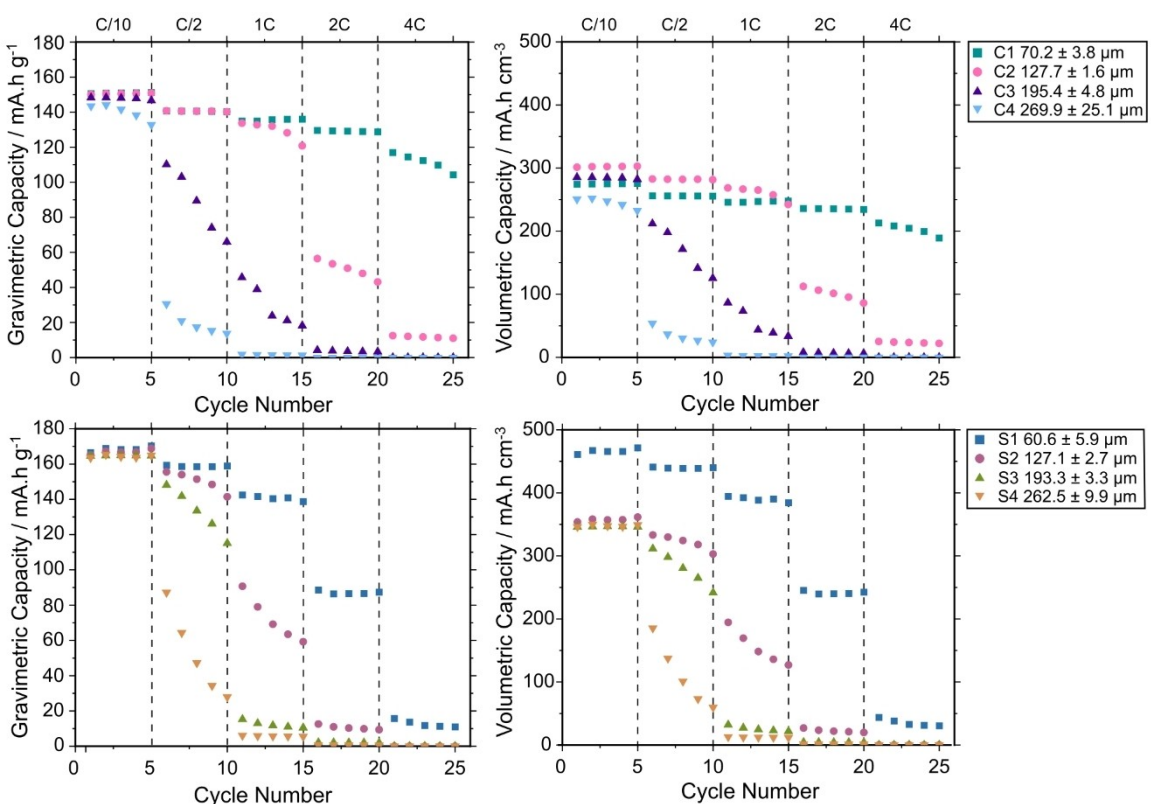


Figure 5. Electrochemical discharge rate capability plots showing average gravimetric (left) and volumetric (right) capacities at C-rates from C/10 to 4 C for formulations C (top) and S (bottom), at a range of thicknesses. Rate capability plots with error bars are shown in Figure S2.

higher in absolute terms than S1, having retained 77.6% of capacity at C/10, compared with 9.5% retention for S1. It is clear therefore that cracking improves volumetric as well as gravimetric performance at C-rates above 1 C for electrodes of moderate thickness.

It is noted that very large standard deviations (Figure S2) are present at C-rates where electrode capacity reduces rapidly, for instance at C/2 for electrode C3. This is coupled with deterioration of capacity over the 5 cycles at the given C-rate. This variation is less pronounced, or not observed at all, where average capacity has dropped to near 0, such as at C/2 for electrode C4. This indicates inconsistency in the C-rate at which cell capacity begins to fail. This may be expected due to the stochastic nature of the cracking process and resultant inconsistent arrangement of cracks. A similar pattern of standard deviations were observed by Lee *et al.*^[48]

This work highlights the potential of mud cracking to improve electrode performance under particular conditions, and it would therefore be desirable to control the formation of cracks. Publications by Lee and Du indicate that the addition of a solvent with a lower surface tension (such as acetone added to NMP, or IPA added to water) allows for some control of crack density, where solvent addition reduces crack size and inter-crack distance.^[46,48] Our work also suggests that other factors of formulation, in particular the relative proportion of conductive additive in relation to the binder, may allow for the tailoring of crack characteristics in combination with the solvent mixture. In addition to tailored crack formation, the response of cracks to calendering and their mechanical stability during cycling, and when tightly wound in commercial cell formats, require further study to evaluate the utility of mud cracking as a means of introducing directional porosity to Li-ion battery electrodes.

Conclusions

In this work, the process of mud cracking in thick Li-ion electrode coatings was studied, and the structures of these cracks were analysed in 2D by optical microscopy, and in 3D with X-ray computed tomography. The trends observed in overall cracking intensity factor and mean crack size were consistent between 2D and 3D data, but the trend in number of cracks as a function of electrode thickness diverged. Thicker electrode coatings were shown to result in wider and deeper cracks, through the full electrode thickness, and larger cracks were correlated with a tendency of crack growth to reduce the size of pores adjacent to the cracked regions. This is reflected in an analysis of the rate performance of cracked electrodes in comparison with conventional uncracked electrodes of equivalent thicknesses. Cracked electrodes of 60–130 µm showed improvements over uncracked electrodes in volumetric and gravimetric discharge capacity at C-rates of 1 C to 4 C, whereas electrodes of 190–270 µm generally performed less well than their uncracked equivalents. Cracks represent directional porous structures which can be introduced to Li ion electrodes without major changes to the manufacturing process, and this work

shows that narrow cracks which do not result in excessive heterogeneity of the pore network should be targeted.

Acknowledgements

The authors would like to acknowledge The Faraday Institution (grant reference FIRG015, FIRG066) for their support in funding this research. PRS acknowledges The Department of Science, Innovation and Technology (DSIT) and the Royal Academy of Engineering under the Chair in Emerging Technologies programme (CiET1718/59)

Conflict of Interests

The authors declare no known competing financial interests or personal relationships which could appear to have influenced the work reported in this paper.

Data Availability Statement

The data that support the findings of this study are available from the corresponding author upon reasonable request.

Keywords: Directional porosity • Electrochemistry • Electrode manufacturing • Lithium ion transport • X-ray computed tomography

- [1] A. J. Ernst, C. R. Wade, D. G. Dyer, D. K. Boakye Danquah, O. S. Tomomewo, *Am. J. Energy Res.* **2023**, *11*, 1–14.
- [2] D. Choi, N. Shamim, A. Crawford, Q. Huang, C. K. Vartanian, V. V. Viswanathan, M. D. Paiss, M. J. E. Alam, D. M. Reed, V. L. Sprenkle, *J. Power Sources* **2021**, *511*, 230419.
- [3] J. Liu, Z. Bao, Y. Cui, E. J. Dufek, J. B. Goodenough, P. Khalifah, Q. Li, B. Y. Liaw, P. Liu, A. Manthiram, Y. S. Meng, V. R. Subramanian, M. F. Toney, V. V. Viswanathan, M. S. Whittingham, J. Xiao, W. Xu, J. Yang, X.-Q. Yang, J.-G. Zhang, *Nat. Energy* **2019**, *4*, 180–186.
- [4] Y. Kuang, C. Chen, D. Kirsch, L. Hu, *Adv. Energy Mater.* **2019**, *9*, 1901457.
- [5] A. M. Boyce, D. J. Cumming, C. Huang, S. P. Zankowski, P. S. Grant, D. J. L. Brett, P. R. Shearing, *ACS Nano* **2021**, *15*, 18624–18632.
- [6] H. Zheng, J. Li, X. Song, G. Liu, V. S. Battaglia, *Electrochim. Acta* **2012**, *71*, 258–265.
- [7] A. M. Boyce, X. Lu, D. J. L. Brett, P. R. Shearing, *J. Power Sources* **2022**, *542*, 231779.
- [8] G. Zhu, D. Luo, X. Chen, J. Yang, H. Zhang, *ACS Nano* **2023**, *17*, 20850–20874.
- [9] C.-J. Bae, C. K. Erdonmez, J. W. Halloran, Y.-M. Chiang, *Adv. Mater.* **2013**, *25*, 1254–1258.
- [10] C. Huang, P. S. Grant, *J. Mater. Chem. A* **2018**, *6*, 14689–14699.
- [11] C. Huang, M. Dontigny, K. Zaghib, P. S. Grant, *J. Mater. Chem. A* **2019**, *7*, 21421–21431.
- [12] B. Delattre, R. Amin, J. Sander, J. De Coninck, A. P. Tomsia, Y.-M. Chiang, *J. Electrochem. Soc.* **2018**, *165*, A388–A395.
- [13] G. Du, Y. Zhou, X. Tian, G. Wu, Y. Xi, S. Zhao, *Appl. Surf. Sci.* **2018**, *453*, 493–501.
- [14] X. Zhang, Z. Ju, L. M. Housel, L. Wang, Y. Zhu, G. Singh, N. Sadique, K. J. Takeuchi, E. S. Takeuchi, A. C. Marsilok, G. Yu, *Nano Lett.* **2019**, *19*, 8255–8261.
- [15] Y. Hwa, E. Yi, H. Shen, Y. Sung, J. Kou, K. Chen, D. Y. Parkinson, M. M. Doeff, E. J. Cairns, *Nano Lett.* **2019**, *19*, 4731–4737.
- [16] D. Dang, Y. Wang, S. Gao, Y.-T. Cheng, *Carbon N. Y.* **2020**, *159*, 133–139.

- [17] S. Yang, C. Zhou, Q. Wang, B. Chen, Y. Zhao, B. Guo, Z. Zhang, X. Gao, R. Chowdhury, H. Wang, C. Lai, N. P. Brandon, B. Wu, X. Liu, *ENERGY Environ. Mater.* **2022**, *5*, 1332–1339.
- [18] Y. Guo, Y. Jiang, Q. Zhang, D. Wan, C. Huang, *J. Power Sources* **2021**, *506*, 230052.
- [19] X. Zhang, Z. Hui, S. King, L. Wang, Z. Ju, J. Wu, K. J. Takeuchi, A. C. Marschilok, A. C. West, E. S. Takeuchi, G. Yu, *Nano Lett.* **2021**, *21*, 5896–5904.
- [20] J. S. Sander, R. M. Erb, L. Li, A. Gurijala, Y.-M. Chiang, *Nat. Energy* **2016**, *1*, 16099.
- [21] J. Billaud, F. Bouville, T. Magrini, C. Villevieille, A. R. Studart, *Nat. Energy* **2016**, *1*, 16097.
- [22] J. Wu, Z. Ju, X. Zhang, X. Xu, K. J. Takeuchi, A. C. Marschilok, E. S. Takeuchi, G. Yu, *ACS Nano* **2022**, *16*, 4805–4812.
- [23] L. Li, R. M. Erb, J. Wang, J. Wang, Y. Chiang, *Adv. Energy Mater.* **2019**, *9*, 1802472.
- [24] H. Wang, J. Li, Z. Miao, K. Huang, Y. Liao, X. Xu, J. Meng, Z. Li, Y. Huang, *ACS Appl. Mater. Interfaces* **2023**, *15*, 26824–26833.
- [25] S. H. Lee, A. Mahadevegowda, C. Huang, J. D. Evans, P. S. Grant, *J. Mater. Chem. A* **2018**, *6*, 13133–13141.
- [26] Y. Zhang, M. Shahriar, S. Hu, *J. Mater. Chem. A* **2023**, *11*, 11849–11858.
- [27] K.-H. Chen, M. J. Namkoong, V. Goel, C. Yang, S. Kazemiannavi, S. M. Mortuza, E. Kazyak, J. Mazumder, K. Thornton, J. Sakamoto, N. P. Dasgupta, *J. Power Sources* **2020**, *471*, 228475.
- [28] W. Pfleging, M. Mangang, Y. Zheng, P. Smyrek, *SPIE Newsroom*, DOI: 10.1117/2.1201602.006342.
- [29] J. B. Habedank, J. Kriegler, M. F. Zaeh, *J. Electrochem. Soc.* **2019**, *166*, A3940–A3949.
- [30] N. A. Dunlap, D. Kern, F. Usseglio-Viretta, D. P. Finegan, B. J. Tremblet de Villers, in *ECS Meeting Abstracts*, The Electrochemical Society, **2021**, DOI: 10.1149/MA2021-023411mtgabs.
- [31] W. Pfleging, R. Kohler, J. Pröll, in *SPIE 8968*, Eds: U. Klotzbach, K. Washio, C. B. Arnold, **2014**, 89680B, DOI: 10.1117/12.2039635.
- [32] C.-S. Tang, C. Zhu, T. Leng, B. Shi, Q. Cheng, H. Zeng, *Eng. Geol.* **2019**, *255*, 1–10.
- [33] W. P. Lee, A. F. Routh, *Langmuir* **2004**, *20*, 9885–9888.
- [34] C. J. Miller, H. Mi, N. Yesiller, *J. Am. Water Resour. Assoc.* **1998**, *34*, 677–686.
- [35] P. Lura, B. Pease, G. B. Mazzotta, F. Rajabipour, J. Weiss, *ACI Mater. J.* **2007**, *104*, 187–194.
- [36] W. Man, W. B. Russel, *Phys. Rev. Lett.* **2008**, *100*, 198302.
- [37] R. C. Chiu, M. J. Cima, *J. Am. Ceram. Soc.* **1993**, *76*, 2769–2777.
- [38] H. Shin, J. C. Santamarina, *Géotechnique* **2011**, *61*, 961–972.
- [39] H. C. W. Parks, A. M. Boyce, A. Wade, T. M. M. Heenan, C. Tan, E. Martínez-Pañeda, P. R. Shearing, D. J. L. Brett, R. Jervis, *J. Mater. Chem. A* **2023**, *11*, 21322–21332.
- [40] A. Wade, A. V. Llewellyn, T. M. M. Heenan, C. Tan, D. J. L. Brett, R. Jervis, P. R. Shearing, *J. Electrochem. Soc.* **2023**, *170*, 070513.
- [41] Y. Mao, X. Wang, S. Xia, K. Zhang, C. Wei, S. Bak, Z. Shadike, X. Liu, Y. Yang, R. Xu, P. Pianetta, S. Ermon, E. Stavitski, K. Zhao, Z. Xu, F. Lin, X. Yang, E. Hu, Y. Liu, *Adv. Funct. Mater.* DOI: 10.1002/adfm.201900247.
- [42] J. Kumberg, M. Müller, R. Diehm, S. Spiegel, C. Wachsmann, W. Bauer, P. Scharfer, W. Schabel, *Energy Technol.* **2019**, *7*, 1900722.
- [43] Y. Wang, D. Dang, D. Li, J. Hu, X. Zhan, Y.-T. Cheng, *J. Power Sources* **2019**, *438*, 226938.
- [44] J. Li, A. K. Dozier, Y. Li, F. Yang, Y.-T. Cheng, *J. Electrochem. Soc.* **2011**, *158*, A689.
- [45] K. B. Singh, M. S. Tirumkudulu, *Phys. Rev. Lett.* **2007**, *98*, 218302.
- [46] Z. Du, K. M. Rollag, J. Li, S. J. An, M. Wood, Y. Sheng, P. P. Mukherjee, C. Daniel, D. L. Wood, *J. Power Sources* **2017**, *354*, 200–206.
- [47] R. Sahore, D. L. Wood, A. Kukay, K. M. Grady, J. Li, I. Belharouak, *ACS Sustain. Chem. Eng.* **2020**, *8*, 3162–3169.
- [48] B.-S. Lee, Z. Wu, V. Petrova, X. Xing, H.-D. Lim, H. Liu, P. Liu, *J. Electrochem. Soc.* DOI: 10.1149/2.0571803jes.
- [49] S. N. Brynteson, A. Kahrom, J. J. Lamb, I. Tolstorebrov, O. S. Burheim, *Batteries* **2023**, *9*, 96.
- [50] K. Rollag, D. Juarez-Robles, Z. Du, D. L. Wood, P. P. Mukherjee, *ACS Appl. Energy Mater.* **2019**, *2*, 4464–4476.
- [51] X. Lu, G. J. Lian, J. Parker, R. Ge, M. K. Sadan, R. M. Smith, D. Cumming, *J. Power Sources* **2024**, *592*, 233916.
- [52] S. Berg, D. Kutra, T. Kroeger, C. N. Straehle, B. X. Kausler, C. Haubold, M. Schiegg, J. Ales, T. Beier, M. Rudy, K. Eren, J. I. Cervantes, B. Xu, F. Beuttenmueller, A. Wolny, C. Zhang, U. Koethe, F. A. Hamprecht, A. Kreshuk, *Nat. Methods* **2019**, *16*, 1226–1232.
- [53] J. J. Bailey, A. Wade, A. M. Boyce, Y. S. Zhang, D. J. L. Brett, P. R. Shearing, *J. Power Sources* **2023**, *557*, 232503.
- [54] F. L. E. Usseglio-Viretta, A. Colclasure, A. N. Mistry, K. P. Y. Claver, F. Pouraghajan, D. P. Finegan, T. M. M. Heenan, D. Abraham, P. P. Mukherjee, D. Wheeler, P. Shearing, S. J. Cooper, K. Smith, *J. Electrochem. Soc.* DOI: 10.1149/2.0731814jes.
- [55] J. Landesfeind, H. A. Gasteiger, *J. Electrochem. Soc.* **2019**, *166*, A3079–A3097.
- [56] L. O. Valgen, J. N. Reimers, *J. Electrochem. Soc.* **2005**, *152*, A882.
- [57] X. Lu, A. Bertei, D. P. Finegan, C. Tan, S. R. Daemi, J. S. Weaving, K. B. O'Regan, T. M. M. Heenan, G. Hinds, E. Kendrick, D. J. L. Brett, P. R. Shearing, *Nat. Commun.* **2020**, *11*, 2079.
- [58] M. Ebner, D.-W. Chung, R. E. García, V. Wood, *Adv. Energy Mater.* **2014**, *4*, 1301278.
- [59] Z. Li, L. Yin, G. S. Mattei, M. R. Cosby, B.-S. Lee, Z. Wu, S.-M. Bak, K. W. Chapman, X.-Q. Yang, P. Liu, P. G. Khalifah, *Chem. Mater.* **2020**, *32*, 6358–6364.

Manuscript received: April 16, 2024

Revised manuscript received: July 9, 2024

Accepted manuscript online: August 17, 2024

Version of record online: October 30, 2024